

PANORAMIC HOLOINTERFEROMETRY

by

Donald R. Matthys
Physics Department
Marquette University
Milwaukee, WI 53233

John A. Gilbert
Dept. of Mechanical & Aerospace Engineering
University of Alabama in Huntsville
Huntsville, AL 35899

Joseph Puliparambil
Physics Department
Marquette University
Milwaukee, WI 53233

ABSTRACT

This paper is the first to report on the quantitative evaluation of panoramic holointerferograms. In the experiment a collinear pair of panoramic annular lenses and an ion laser are used to illuminate and observe the inner walls of a circular pipe. A hologram is taken of the wall surface with the object beam being introduced exterior to the imaging system. The resulting holographic image is in the shape of an annulus showing the entire surround of the lenses over a belt approximately 50° wide front to back. To produce the holointerferogram, a carrier is introduced by translating the pipe axially, and a line load is applied parallel to the system axis. The interference pattern of the carrier and deformation is then recorded with a CCD. This pattern is analyzed in the usual way (phase mapping, carrier subtraction, phase unwrapping) only after the pattern is linearized by applying a two-dimensional mapping to correct the distortions introduced by the panoramic optical system. The experimental results are excellent and demonstrate the unique value of panoramic annular lenses in making precision deformation mappings of the interior surface of pipes or cylinders.

INTRODUCTION

Several papers on the topic of radial metrology have been presented earlier on the use of a special panoramic annular lens (PAL) to make visual observations and/or precision measurements on the interior surfaces of rings or pipes.¹⁻¹² Although a few of those earlier papers have shown the feasibility of making interferometric measurements with a PAL,^{3,10,12} this paper is the first to report on the quantitative evaluation of panoramic holointerferograms.

Panoramic holointerferometry refers to the process of making a 360° double-exposure, real-time or time-averaged hologram of the inside of a cylindrical cavity wall using a panoramic annular lens. The PAL consists of a single piece of glass with spherical surfaces that produces a flat annular image of the entire surround of the optical axis of the lens with a field of view extending from about 45° off-axis to about 100° off-axis. A standard PAL imaging system is shown in Figure 1; Figure 2 shows the geometric structure of the PAL by itself. A virtual image is formed inside the PAL by a combination of reflection and refraction; thick lines shown in Figure 2 indicate reflecting surfaces. Since the PAL forms a virtual image, a transfer lens must be employed to transfer the image to a sensor. The PAL is almost afocal, and obtains an image from right up against the lens surface out to infinity. Objects to the front of the lens are imaged to the

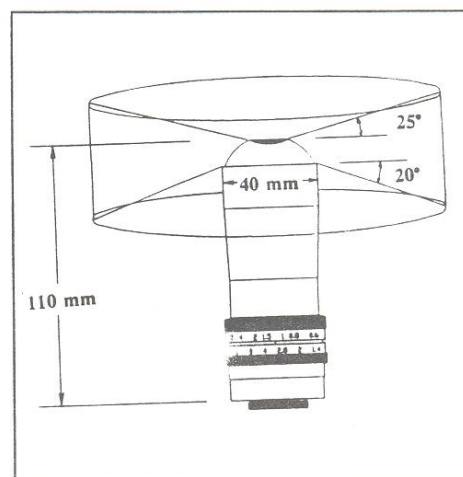


Figure 1. A 38 mm diameter PAL imaging system. Figure provided courtesy of Optechnology, Inc., Huntsville, AL.

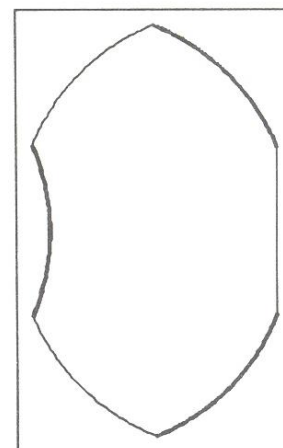


Figure 2. Physical shape of a PAL.

interior of the annulus and objects to the rear of the lens appear on the outer part of the annulus.

Direct visual interpretation of a PAL image is sometimes confusing for the unskilled observer and algorithms have been developed to allow the annular shaped images to be linearized for viewing and measuring purposes. The mapping used for this purpose maintains equal maximal dimensions by 'rolling' the annular image along its outer circumference and moving all the pixels between the contact point and the center of the image to a vertical line in the final rectangular image.⁹ Next, because the annular image is not linear in the radial direction, a vertical stretching of the rectangular image is performed.¹³

This paper demonstrates that the PAL system and the linearization algorithms can be combined with the carrier fringe method and phase unwrapping to perform quantitative analysis on panoramic holographic interferograms. The experimental results are excellent and demonstrate the unique value of a PAL in making precision deformation mappings of the interior surface of pipes or cylinders.

HOLOGRAPHIC ANALYSIS

In Figure 3, it is assumed that two opposing collinear PALs are aligned with their optical axes along the z direction; Cartesian (x,y,z) and cylindrical (r,θ,z) coordinate systems can be used to describe the object space. Coherent light is projected by one PAL from the source point S to a point P located on the inner wall of a cylindrical cavity. The image of P is observed by the second PAL at point O . To enable mathematical analysis, unit vectors \hat{e}_1 and \hat{e}_2 are shown in the direction of illumination and in the direction of observation, respectively. These vectors help in analyzing the holographic fringes produced when the reconstructed holographic image corresponding to an undeformed object and the same deformed surface are superposed. The change in path length between the two holographic recordings gives rise to a distribution of phase differences between the reconstructed wavefronts which results in areas of constructive or destructive interference and is seen as a set of light and dark fringes.

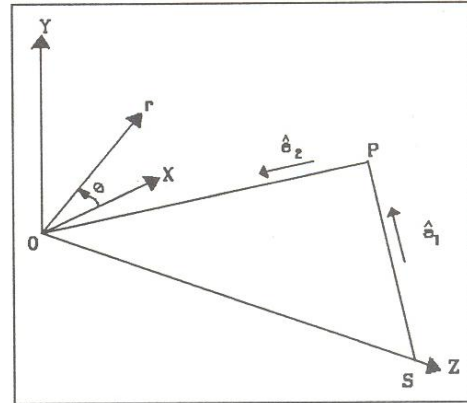


Figure 3. Cartesian (x,y,z) and cylindrical (r,θ,z) coordinate systems used to describe object space.

For the case shown in Figure 3, the locations of fringes produced by this superposition are given by

$$n\lambda = (\hat{e}_2 - \hat{e}_1) \cdot \mathbf{d} = \mathbf{g} \cdot \mathbf{d} \quad (1)$$

where n is the fringe order number and λ is the wavelength of the coherent light used to record and reconstruct the hologram. The component of displacement measured at each point depends upon the location of the source and on the point of observation; the displacement vector \mathbf{d} is projected along the sensitivity vector \mathbf{g} which lies along the angle bisector of \hat{e}_1 and \hat{e}_2 . In general, the sensitivity vector lies along a different direction for each point in the field of view.

Although Equation (1) yields the magnitude of the component of \mathbf{d} along the direction of \mathbf{g} , its sign is uncertain. This sign ambiguity is troublesome and must be confronted in the data analysis. One approach is demonstrated in this paper; carrier fringes are introduced into a holographic interferogram produced by deforming a circular pipe. The superposition produces a monotonically changing phase distribution along the interferogram. The sign of the displacement component is obtained when the carrier fringe pattern is subtracted from the holographic interferogram in the spatial frequency domain.

EXPERIMENTAL

Experiments were performed on a vibration isolated table with the setup shown in Figure 4. Two 38 mm (1.5") diameter PALs were spaced at a distance of 3.175 mm (0.125") apart and positioned with their optical axes aligned with the z axis of the coordinate system (see Figure 3). A circular aluminum pipe with an inner radius R equal to 69.85 mm (2.75") and a wall thickness of 3.0 mm (0.117"), was mounted on a kinematic stage and positioned around the PALs with its longitudinal axis also along z . The inner surface of the pipe was painted white and then the pipe was placed in such a way that the two PALs could be centered inside it. Coherent light ($\lambda = 514$ nm) was projected onto the inner wall of a 50.8 mm (2.0") long section of the pipe using a collimated beam passed through one of the PALs. An image

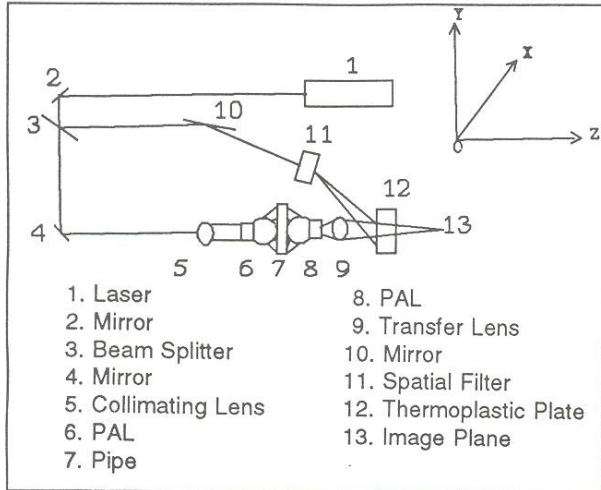


Figure 4. Experimental setup for recording real-time holograms. A CCD camera is used to acquire images.

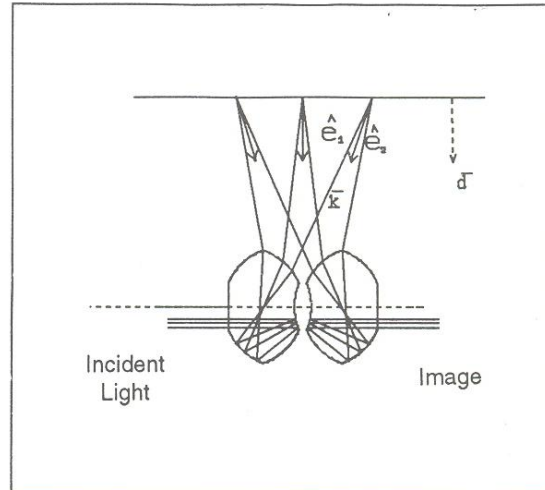


Figure 5. Figure to show the direction of the sensitivity vectors.

of the pipe in its initial position was captured using a second PAL. A collector lens was used to convey the virtual image formed within the second PAL to a CCD camera and computer system. The reference beam reflected by the beam splitter was expanded through a spatial filter onto a thermoplastic holocamera positioned behind the collector lens.

Since the angle between the incident and the transmitted ray varies from +15 degrees to -15 degrees across the field of view, the direction of the sensitivity vector changes along the length of the pipe. This is illustrated in Figure 5 which shows the sensitivity vectors for points located in the center and at the ends of the field of view. Figure 6 shows the fringe pattern recorded when the pipe was translated axially along the z -axis, through a displacement w equal to 0.0038 mm (0.00015"). In this case, a zero order fringe coincides with the path around the middle of the annular ring where the sensitivity vector is perpendicular to the displacement. The phase monotonically changes across the field of view.

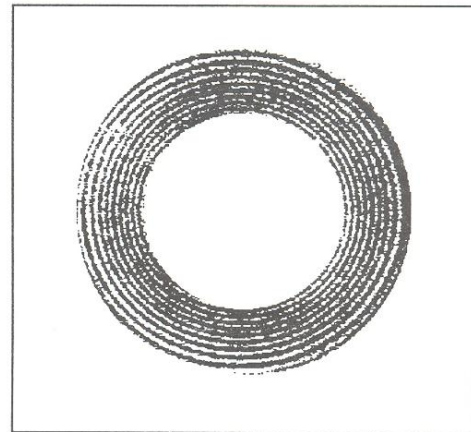


Figure 6. Panoramic holointerferogram recorded when the pipe is translated in the axial z direction through 0.0038 mm.

Figure 7, on the other hand, shows an interferogram obtained when a vertical diametral load of 51 grams is applied to the pipe. The interpretation of this pattern requires the application of standard interferometric analysis techniques such as phase shifting and phase stepping methods, heterodyne holographic interferometry or carrier fringe methods. Since the distortions inherent in the PAL image make this process difficult, they must be removed by the linearization procedure described earlier. Moreover, many of the standard fringe analysis techniques will fail in those cases where the fringes form a closed loop because the same fringe will be encountered twice in going from one end of the interferogram to the other. This problem can be eliminated using the method of carrier fringes. The following section demonstrates how image linearization and the carrier fringe method are used to obtain quantitative results for the deformation inherent in Figure 7.

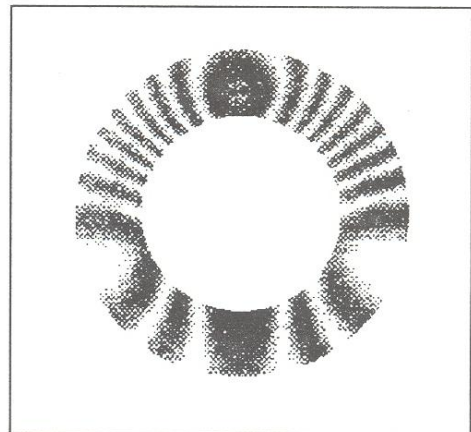


Figure 7. Panoramic holointerferogram obtained by applying a vertical compression to the pipe by loading it with 51 grams.

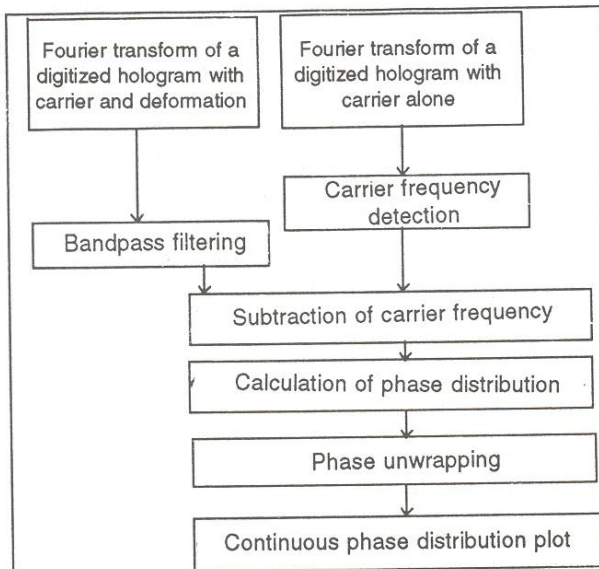


Figure 8. Flow Chart for phase unwrapping.



Figure 9. Fringe pattern obtained when the pipe is subjected to diametral compression along with a translation in the axial z direction.

DATA ANALYSIS

A combination of image digitization, image processing, two-dimensional fast Fourier transformation and subsequent computerized analysis is used in the data analysis. The procedure is given in the flow chart shown in Figure 8.¹⁴ The quantitative evaluation of the interference patterns mainly consists of the pointwise determination of the interference phase and of the sensitivity vectors. From the interference phase distribution and the sensitivity vectors, which are given by the geometrical arrangement of the optical components in the holographic setup, the displacement field is calculated. The method of carrier fringes makes use of the properties of Fourier transform to achieve this. The automated data analysis is done with the help of the PL2500 Array Processor (by Eighteen and Eight Laboratory) and the Image-Pro Plus image processing system (by Media Cybernetics, Inc.).

The first step is to produce an interferogram having a monotonically changing phase distribution. This may be accomplished for the loaded pipe by superimposing the phase distributions corresponding to a carrier pattern, produced by translating the pipe along the z -axis (see Figure 6), with the deformation produced by loading it (see Figure 7). The resulting panoramic holointerferogram is shown in Figure 9. The next step is to apply the linearization algorithms; the first quadrants of the images shown in Figures 6 and 9 are shown in Figures 10 and 11, respectively.

After linearizing the holointerferograms corresponding to the carrier and the carrier plus the deformation, the Fourier transform is applied to each of their quadrants. Each quadrant image is 295 pixels wide and 134 pixels high. The PL2500 array processor requires the signal to be a square array to apply the Fourier Transform. So each quadrant is placed at the center of a square array of 512 x 512 video screen and saved into a file. This is done using the ImagePro software program. All the pixels surrounding the quadrant are filled with zeros. This is illustrated in Figure 12 for the fringe pattern shown in Figure 11.

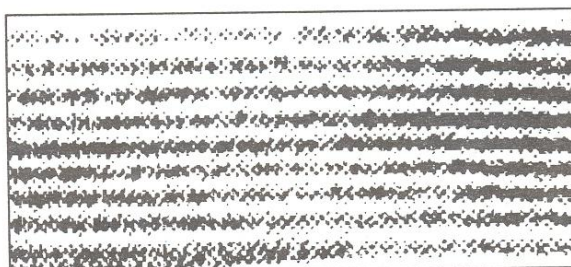


Figure 10. Linearized first quadrant of Figure 6.



Figure 11. Linearized first quadrant of Figure 9.

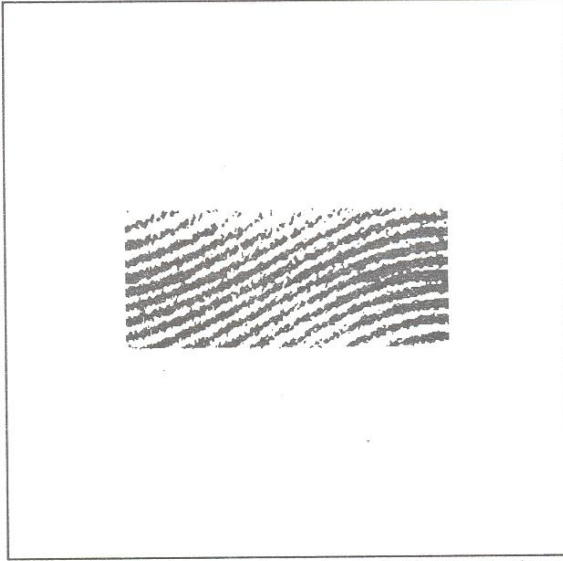


Figure 12. The fringe pattern shown in Figure 11 placed at the center of a 512 x 512 square grid, in preparation for a Fourier transform.

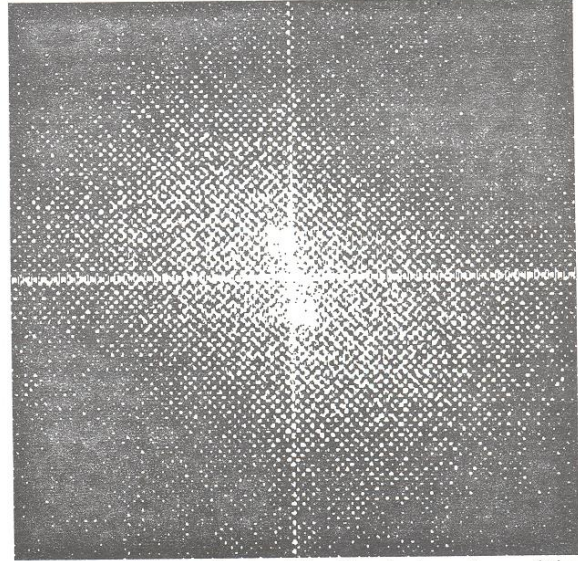


Figure 13 The amplitude of the Fourier transform of the first quadrant as shown in Figure 12.

For direct FFTs, the input image file contains raw data in 8-bit unsigned integer format, while the PL2500 works on 32-bit floating point format. So the data format has to be converted after the data is transferred from the host PC to the PL2500 array processor. For a complex Fourier transform, the data should also be converted to complex values by inserting imaginary values of zero to form a complex data array for the FFT. For visual presentation, the data is shifted to move the origin of the spatial frequency domain to the center of the array. Figure 13 shows the amplitude spectrum of the Fourier transform of the interferogram in Figure 12.

The intensity distribution of a carrier modulated holographic interferogram is described by

$$I(x,y) = a(x,y) + b(x,y) \cos [2\pi f_0 y + \phi(x,y)] . \quad (2)$$

The cosine function can be expressed in the following form by Euler's formula:

$$\cos \theta = \frac{[\exp (j\theta) + \exp (-j\theta)]}{2} \quad (3)$$

so Equation (2) can be rewritten as:

$$I(x,y) = a(x,y) + c(x,y) \exp (2\pi j f_0 y) + c^*(x,y) \exp (-2\pi j f_0 y) \quad (4)$$

where

$$c(x,y) = b(x,y) \frac{\exp [j\phi(x,y)]}{2} \quad (5)$$

and $c^*(x,y)$ is the complex conjugate of $c(x,y)$.

After a two-dimensional Fourier transform is applied to Equation (3), the spatial frequency distribution of the intensity $I(x,y)$ can be represented in Fourier space as:

$$I(u,v) = A(u,v) + C(u,v-f_0) + C^*(u,v+f_0) \quad (6)$$

where $A(u,v)$ represents the background irradiance which varies slowly with location in comparison with the fringe spacing; $C(u,v)$ and $C^*(u,v)$ are placed symmetrically with respect to the origin, and contain the desired information.

In the spatial frequency domain, $A(u,v)$ and $C^*(u,v)$ can be cut off by using a bandpass filtering technique. The transfer function of a practical applied band-pass filter has the form:

$$H(u,v) = \begin{cases} 1 & 0 < u < u_c, \quad |v| < v_c \\ 0 & \text{otherwise} \end{cases} \quad (7)$$

where u_c and v_c are user-defined cut-off frequencies of the regular bandpass filter in the horizontal and vertical directions, respectively. With the band-pass filtering techniques it is possible to obtain the information needed in the frequency domain and get rid of the high frequency speckle noise and low frequency DC components.¹⁵

The carrier frequency is located by scanning the spectra in the spatial frequency domain of the interferogram containing the carrier alone. $C(u,v-f_0)$ is shifted to the origin by f_0 . In order to further improve the quality of the image by eliminating Gaussian irradiance and speckle noise, a band-pass filter is applied in the spatial frequency domain. The inverse Fourier transform of $C(u,v)$ generates complex $c(x,y)$ with real and imaginary parts. Figure 14 shows the spectrum after bandpass filtering and shifting by the amount of the carrier frequency.

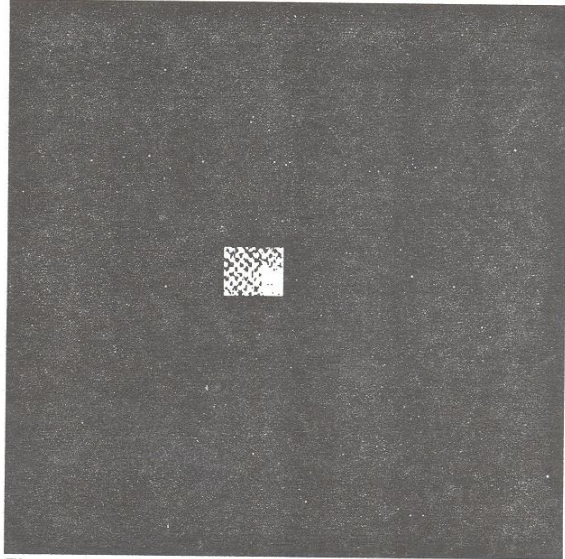


Figure 14. The amplitude spectrum of Figure 13 after bandpass filtering and shifting.

After the inverse FFT, the origin of spatial frequency domain is shifted from the center of the array back to the corner of the array. The desired interference phase $\phi(x,y)$ can be calculated by:

$$\phi(x,y) = \arctan \frac{\text{Im } c(x,y)}{\text{Re } c(x,y)} \quad (8)$$

where $\text{Re } c(x,y)$ and $\text{Im } c(x,y)$ refer to the real and imaginary parts of $c(x,y)$. The pointwise phase computation is performed by using the PL2500 array processor according to Equation (8).

Due to the function $\arctan()$ calculated by the computer, the value of $\phi(x,y)$ is always within the range from minus to plus π . This phase discontinuity must be corrected by using a phase unwrapping algorithm.¹⁵ Phase unwrapping algorithms are widely used in fringe analysis and based on the following two assumptions: (1) the phase distribution due to the surface deformation of the test object is assumed to be continuous, and (2) there are at least two pixels per fringe at the highest spatial frequency.

Since the variation of phase is slow compared with the sampling interval, the absolute value of the phase difference between adjacent pixels is much less than π at points where the phase difference is continuous. But it becomes greater than π at points where the 2π phase jump occurs.

The discontinuous phase is plotted in Figure 15. The phase difference between two adjacent pixels can be calculated by

$$\Delta\phi_d(x_i, y) = \phi_d(x_i, y) - \phi_d(x_{i-1}, y) \quad (9)$$

where the subscript i denotes the i th pixel and $i-1$ the point preceding it. The range of i runs from 1 to $N-1$ to cover all the pixels. To find the position of discontinuities in the phase distribution, an appropriate criterion for the absolute phase difference (e.g. π) is set. If at some point $|\Delta\phi_d(x_i, y)| > \pi$, that point is located at a phase jump. The direction of the jump can be determined by the sign of $\Delta\phi_d(x_i, y)$.

The discontinuous phase $\phi_d(x,y)$ can be corrected by adding an offset phase distribution $\phi_0(x,y)$ to obtain a continuous distribution $\phi_c(x,y)$

$$\phi_d(x,y) = \phi_d(x,y) + \phi_o(x,y) . \quad (10)$$

The offset phase at every pixel is calculated along each row starting from the point $x = 0$. Because only a relative phase distribution needs to be determined, the offset phase at the first sample point in the row ($x = 0$) is set equal to zero, i.e. $\phi_o^x(x_0,y) = 0$, where the superscript x denotes phase unwrapping in the x direction. Then

$$\phi_o^x(x,y) = \phi_o^x(x_0,y) \quad (11)$$

for $i = 1, 2, \dots, k-1$ until the first phase jump is detected at the k th sample point. If the direction of the phase jump (i.e., $\phi_d(x_k,y) > \pi$) is positive, then

$$\phi_o^x(x_k,y) = \phi_o^x(x_{k-1},y) - 2\pi \quad (12)$$

whereas, if the jump is negative (i.e., $\phi_d(x_k,y) < -\pi$) then

$$\phi_o^x(x_k,y) = \phi_o^x(x_{k-1},y) + 2\pi . \quad (13)$$

At those points where there is no phase discontinuity,

$$\phi_o^x(x,y) = \phi_o^x(x,y) \quad (14)$$

for $i = k+1, i = k+2, \dots, i = m-1$, until the next jump occurs at the m th sample point. The criterion for phase difference is then applied to the m th sample point and either Equation (12) or (13) is used depending upon the condition being satisfied. These procedures of addition or subtraction of phase 2π are repeated along each row of the image to obtain the phase offset of each row $\phi_o^x(x,y)$. By adding this offset to the discontinuous phase distribution $\phi_d^x(x,y)$, a continuous phase distribution $\phi_c^x(x,y)$ for each row is obtained. Because $\phi_o^x(x_0,y) = 0$ is set at the beginning of each row regardless of the phase distribution in the y direction, it is now necessary to perform phase unwrapping in the y direction. Based on the phase unwrapping in the x direction, it is sufficient to choose one arbitrary column $x = x_L$ to determine the phase offset $\phi_o^y(x,y)$ along the y direction. This can be done by the same procedure as in the x direction with the initial setting $\phi_o^y(x_L,y) = 0$.

The offset phase of a two-dimensional image is then given by

$$\phi_o(x,y) = \phi_o^x(x,y) - \phi_o^x(x_L,y) + \phi_o^y(x_L,y) . \quad (15)$$

In the above equation, $\phi_o^x(x,y) - \phi_o^x(x_L,y)$ represents the difference of the offset phase between the points (x,y) and (x_L,y) , and $\phi_o^y(x_L,y)$ is the difference of the offset phase between the points of (x_L,y) and (x_L,y_0) , so that $\phi_o(x,y)$ gives a relative offset phase distribution defined as the difference from the initial value at (x_0, y_0) .

This phase unwrapping algorithm is applied to the phase map obtained after the Fourier transform, bandpass filtering, and inverse Fourier transform of each of the quadrants is performed. Figure 16, for example, shows the phase map in the middle portion of the first quadrant after complete phase wrapping is done. Two-dimensional phase maps can also be plotted for the entire surface of each of the four quadrants and they show the displacement values on the inside surface of the pipe due to the applied load. Figure 17 shows the phase map of the first quadrant.

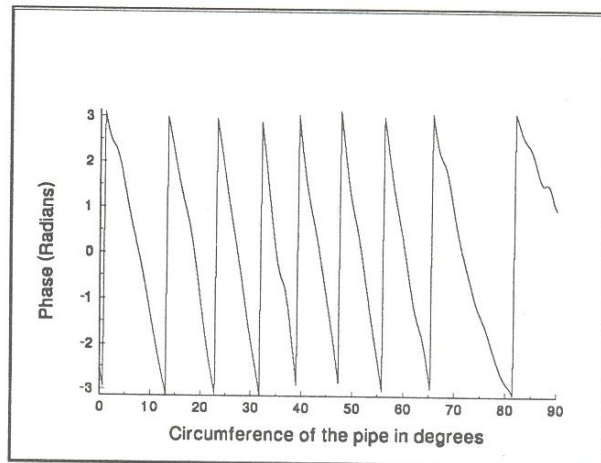


Figure 15. The phase map in the middle of the pipe along the circumference of the pipe before phase unwrapping.

In order to show the displacement values inside the entire pipe the information from all four quadrants need to be joined together. Figure 18 shows how the interferogram would look when the four quadrants are joined. This figure is made by changing the aspect ratio; the height of the picture is stretched so that it is possible to observe the overall shape of the linearized holointerferogram.

Actually, the phase unwrapping can be done manually since the fringe pattern is rather simple. The zero order fringe is assigned to the point where the contact point between the surface and the pipe is located. At this point there is no displacement of the pipe. This occurs at the 270° point on the circumference of the pipe. The third fringe from the top on this 270° point is selected for analysis and designated the zero order fringe. Its location is marked on Figure 18 by a small circle. The fringes below it are numbered with increasing negative numbers and the fringes above it are numbered with increasing positive numbers. Now a horizontal line is drawn through the figure just touching the top of the chosen fringe at 270° . The total angle inside the cavity is 360° . At every 10° , the number of the fringe which crosses the horizontal line is recorded. A graph is drawn with the circumference of the pipe in degrees as abscissae and with fringe order numbers as ordinates. Figure 19 shows the phase map of the inside surface of the pipe around its circumference, the circumference of the pipe being in degrees. From this the nature of the displacement values around the circumference of the pipe is seen.

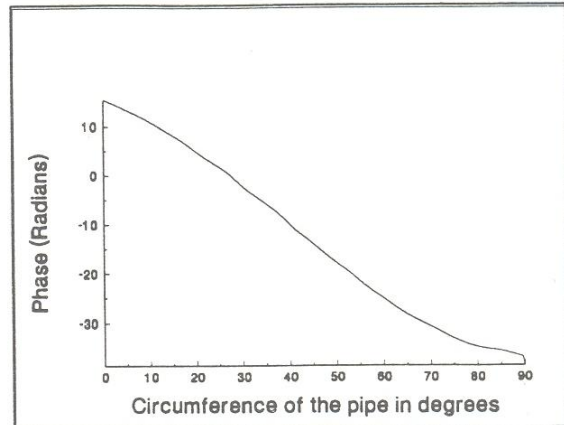


Figure 16. The phase map of the middle portion of the first quadrant after complete phase unwrapping is done.

If the fringes were more complex in nature, it would have been very difficult to apply this method. So there is a need for automating this process. In order to do that, phase unwrapping is done and then the results for each of the four quadrants are joined together. However, a linearized image of the complete surface pipe is 1080 pixels and it is not feasible to display that big an image on most computer monitors as they do not have that much resolution. So the analysis is done a quadrant at a time and then the results are joined together after the phase unwrapping to view the 360° surround of the inner cavity surface.

The deformations caused by the diametral compression due to the metal bar are of the order of a few wavelengths of light. So they cannot be plotted in their actual dimensions. They have to be multiplied by a scaling factor and then the shape of the deformation can be studied.

To demonstrate the shape of the pipe after deformation, it is assumed that the pipe is originally circular and can be represented by a circle of radius 5.08 cm (2"). If the deformation is magnified, then it can be superposed on this circle. It is seen in Figure 19 that the maximum deformation produces a phase change of less than 50 radians. That value is taken as the maximum deformation. So to scale the maximum deformation to 6.35 mm (0.25") a scale factor of $6.35 \text{ mm}/50 \text{ radians}$ ($0.25"/50 \text{ radians}$) is chosen. Now each phase change value on the circumference of the pipe as obtained from the phase unwrapping procedure is multiplied by this factor. Each of these values is either subtracted or added to the radius of the circle depending on the sign of the change. These values are plotted and the result is shown in Figure 20. In Figure 20, it is seen that the maximum vertical displacement occurs at the top and there is no displacement at the bottom where the pipe is in contact with the surface. On the other hand, the maximum horizontal displacement occurs at about 10° below the original center of the pipe.

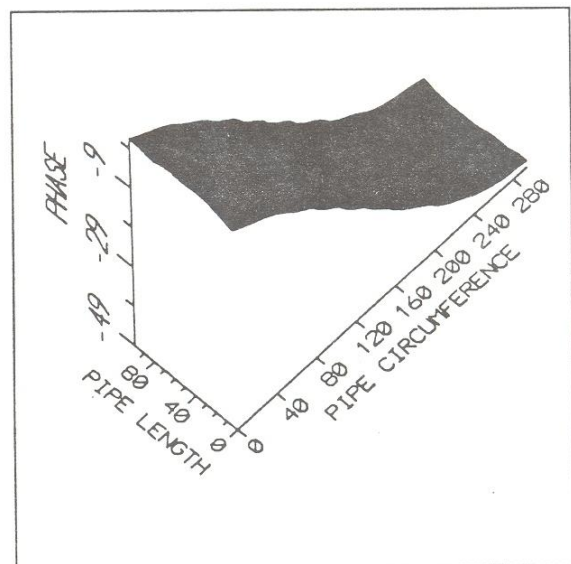


Figure 17. Phase map of the first quadrant.

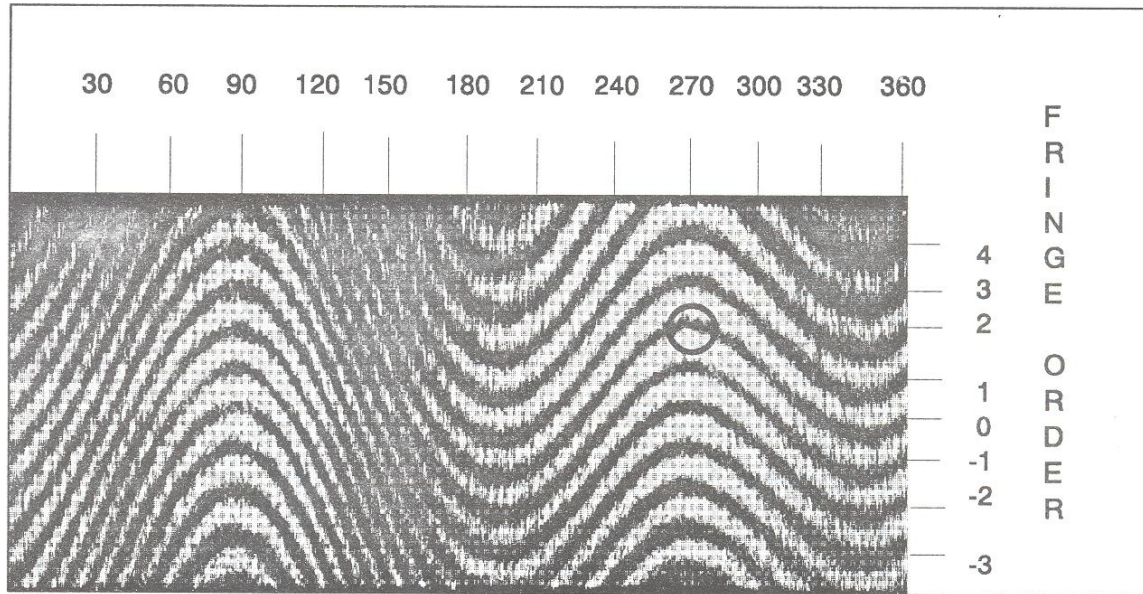


Figure 18. An overall view of all the four quadrants joined together. Circle at 270 degrees indicates fringe selected as zero order.

Now from the phase unwrapping results it is found that the maximum phase change is 38.2 radians. For points in the image where the sensitivity vector is radial, the displacement u_r is

$$u_r = \frac{\Delta \phi \lambda}{4\pi \cos \theta} \quad (16)$$

where 2θ is the angle between the propagation vectors in the direction of illumination and observation.

For the middle portion of the pipe the angle between these vectors is approximately 15° and the maximum deformation of the pipe as 1576.77 nanometers. Roark¹⁶ discusses the deformation of a pipe that is subjected to diametral compression. The ratio of the change in the vertical to the change in the horizontal diameter is given as -1.0893. If the phase shifts shown in Figure 20 are converted to displacements using Equation (16), this ratio is -1.0852. The percentage of error from the theoretical value is less than 1%. The shape of the deformed section also agrees with that determined using artificial speckle and the method of digital correlation.⁶

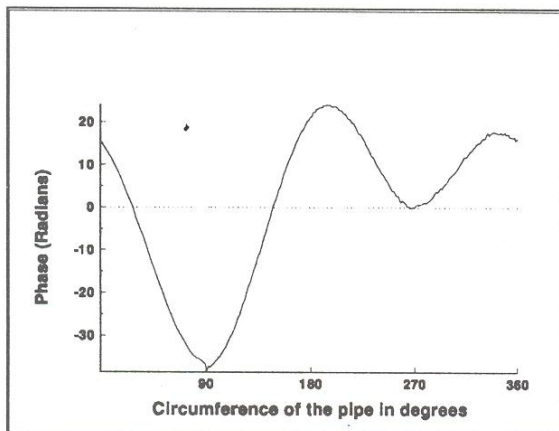


Figure 19. Phase plot at the middle of the pipe around its circumference in degrees. Dotted line represents undeformed surface.

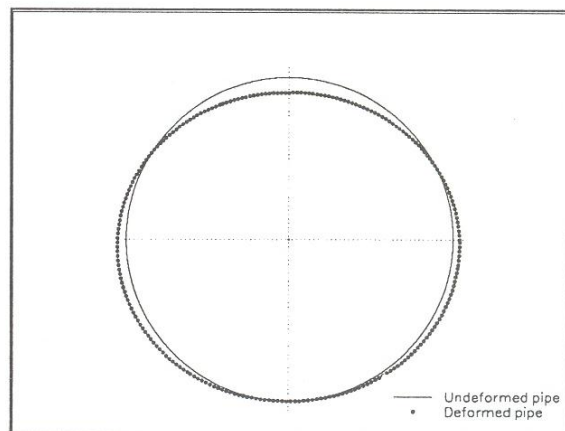


Figure 20. Deformation of the pipe around its circumference. The deformation is exaggerated to make it make it visible.

In the section on holographic analysis, the effect of the sensitivity vector was discussed. Since the sensitivity vector is found to be $\mp = 15^\circ$ i.e., the sensitivity vector changes across the field of view from $+15^\circ$ in the front to -15° at the back, introducing an error factor ($\cos \theta$) into the radial displacement measurement. This error factor is maximum at the edges of the field of view where it is $(1 - \cos 15^\circ)$, or 4%. At the center of the field of view where the sensitivity vector is vertical the error becomes zero. This error factor does not affect the way Roark's formulas are applied in this case, since Roark's result is a ratio which experiences the same change in both the denominator and numerator.

CONCLUSIONS

This paper has demonstrated that the method of phase unwrapping can be applied to obtain quantitative results from panoramic holo-interferograms. The process uses an array processor along with a computer and is applied to linearized quadrants of panoramic images. These are later joined together to study the displacement field. The experimental results are consistent with theory and demonstrate the unique value of a PAL in making precision deformation mappings of the interior surface of pipes of cylinders.

REFERENCES

1. Gilbert, J.A., Greguss, P., Lehner, D.L., Lindner, J.L., "Radial profilometry," Proc. of the Joint BSSM/SEM International Conference on Advanced Strain Measurement Techniques, London, England, August 24-27, 1987, Whittles Publishing, pp. 97-107.
2. Greguss, P., Gilbert, J.A., Matthys, D.R., Lehner, D.L., "Developments in radial metrology," Proc. of SPIE International Symposium on Optical Engineering and Industrial Sensing for Advanced Manufacturing Technologies, Vol. 954, Dearborn, Michigan, June 25-30, 1988, pp. 392-398.
3. Gilbert, J.A., Greguss, P., Kransteuber, A.S., "Holo-interferometric patterns recorded through a panoramic annular lens," Proc. of SPIE's International UNESCO Seminar on 3-D Holography, Volume 1238, entitled 3-D Holography '89, Kiev, USSR, September 5-8, 1989.
4. Matthys, D.R., Greguss, P., Gilbert, J.A., Lehner, D.L., Kransteuber, A.S., "Radial metrology with a panoramic annular lens," Proc. of SPIE's 33rd. Annual International Symposium on Optical & Optoelectronic Applied Science & Engineering, San Diego, California, August 6-11, 1989.
5. Gilbert, J.A., Matthys, D.R., Greguss, P., "Optical measurements through panoramic imaging systems," Proc. of the 1990 Int. Conf. on Hologram Interferometry & Speckle Metrology, Baltimore, Maryland, November 4-7, 1990, pp. 164-171.
6. Matthys, D.R., Gilbert, J.A., Greguss, P., "Endoscopic measurement using radial metrology with digital correlation," Optical Engineering, 30(10): 1455-1460 (1991).
7. Gilbert, J.A., Matthys, D.R., Lehner, D.L., Hendren, C.M., "Panoramic imaging systems for nondestructive evaluation," Proc. of the Third Conference on Nondestructive Evaluation for Aerospace Requirements, Huntsville, Alabama, June 4-6, 1991.
8. Gilbert, J.A., Matthys, D.R., Lehner, D.L., "Moire measurements using a panoramic annular lens," Proc. of SPIE's 1991 International Symposium on Optical & Optoelectronic Applied Science & Engineering, San Diego, California, July 21-26, 1991, pp. 202-209.
9. Matthys, D.R., Gilbert, J.A., Puliparambil, J., "Endoscopic inspection using a panoramic annular lens," Proc. of SPIE's 1991 International Symposium on Optical & Optoelectronic Applied Science & Engineering, San Diego, California, July 21-26, 1991, pp. 736-742.
10. Gilbert, J.A., Matthys, D.R., Hendren, C.M., "Displacement analysis of the interior walls of a pipe using panoramic holo-interferometry," Proc. of SPIE's 1991 International Symposium on Optical & Optoelectronic Applied Science & Engineering, San Diego, California, July 21-26, 1991, pp. 128-134.
11. Beshears, R.D., Gilbert, J.A., Matthys, D.R., "Non-destructive examination of rocket motor components," Proc. of the 1992 Conference on Advanced Earth-To-Orbit Propulsion Technology, Huntsville, AL, May 19-21, 1992.
12. Lindner, J.L., Gilbert, J.A., "Modal holographic interferometry utilizing the panoramic annular lens," Proc. of the 11th International Modal Analysis Conference (IMAC), Kissimmee, Florida, February 1-4, 1993.
13. Puliparambil, J., "Panoramic imaging and holographic interferometry using a panoramic annular lens," Doctoral Dissertation, Marquette University, Physics Department, Milwaukee, WI, 1982, pp. 24-36.
14. Guo, D., "Automated evaluation of holographic interferograms by combining Fourier transform and phase shift techniques," Master's Thesis, Marquette University, Physics Department, Milwaukee, WI, 1989, pp. 34-37.
15. Takeda, M., Ina, H., Kobayashi, S., "Fourier transform method of fringe-pattern analysis for computer-based topography and interferometry," Journal of the Optical Society of America, 72: 156-160 (1982).
16. Young, W., Roark's Formulas for Stress and Strain, pp. 262-263, McGraw-Hill, New York, 1989.